energies

MDPI

Article

Remnant Magnetisation State Control for Positioning of a Hybrid Tunable Magnet Actuator

Endre Ronaes, Andres Hunt and Hassan HosseinNia *

Department of Precision and Microsystems Engineering, TU Delft, Mekelweg 2, 2628 CD Delft, The Netherlands; e.p.ronaes@tudelft.nl (E.R.); a.hunt@tudelft.nl (A.H.)
* Correspondence: s.h.hosseinniakani@tudelft.nl

Abstract: The recent development of a hybrid tunable magnet actuator proposes to eliminate Joule heating when maintaining a force or position offset. By controlling the remnant magnetic flux in an AlNiCo magnet within the actuator, the actuation force can be linearly varied and maintained. While a method for tuning the magnetisation state of the magnet with minimal magnetic field changes has been demonstrated previously, the method is inefficient due to its slow tuning rate, which hinders its use in controlling the actuator's position. This paper presents a novel method of magnetisation state tuning with a fast tuning rate and validates its effectiveness for controlling the position of a short-stroke linear actuator. This tuning method is implemented and verified for changing the flux density of an AlNiCo magnet in the range of ±1.2 T, with a root-mean-square error (RMSE) of 7.2 mT. An accurate estimation of the magnetisation state is furthermore achieved during positioning, guided by the design and experimental validation of a lumped parameter model, allowing the position to be controlled with an RMSE of 4.0 µm in a range of −157 to 320 µm.

Keywords: reluctance actuators; in situ magnetisation; quasi-static positioning

check for updates

Citation: Ronaes, E.; Hunt, A.; HosseinNia, H. Remnant Magnetisation State Control for Positioning of a Hybrid Tunable Magnet Actuator. *Energies* **2023**, *16*, 4548. https://doi.org/10.3390/en16124548

Academic Editors: Mauro Andriollo and Andrea Tortella

Received: 9 May 2023
Revised: 29 May 2023
Accepted: 2 June 2023
Published: 6 June 2023

Copyright: © 2023 by the authors. Licensee MDPI, Basel, Switzerland. This article is an open access article distributed under the terms and conditions of the Creative Commons Attribution (CC BY) license (https://creativecommons.org/licenses/by/4.0/).

1. Introduction

The need for high accelerations in electromagnetically actuated high-precision linear stages must be weighed against their influence on the thermal stability of the system and, thereby, on its accuracy and repeatability. Coil-based actuators are often favoured in precise positioning stages due to their low stiffness behaviour and, hence, their ability to attenuate low-frequency disturbances [1,2]. However, the production of Joule heating during sustained forces may incur significant positioning errors as a result of thermal expansion [3,4].

The desire for both high accuracy and throughput, combined with limited design space for the dissipation of heat, has led to an increased interest in utilising reluctance actuators (RAs) for short-stroke stages. This is due to the RAs' higher force density and efficiency compared to the more commonly used voice coil actuators [1,5,6]. To compensate for the non-linear current–force and position–force dependencies, magnetic hysteresis, and eddy current damping, a concerted effort has lead the development of new control strategies and RA topologies [5,7]. To roughly linearise the current– and position–force dynamics, hybrid reluctance actuator (HRA) designs introduce bias flux paths in the RA architecture by integrating high-coercive-force (HCF) permanent magnets (PMs) [1,7]. For many applications, such as in magnetic bearings [8] and fast steering mirrors [9], this provides a sufficient efficiency and acceleration while also providing good accuracy and repeatability through linear feedback control. Nevertheless, in systems requiring a maintained position or force offset, such as in a gravity compensator with a fixed PM arrangement, the resulting continuous energy dissipation from HRA stages remains problematic [4].

To remove continuous heat dissipation in such quasi-static loading regimes, Hüffner et al. designed a gravity compensator on the conceptual basis of the electropermanent actuator

developed in [10] with a low-coercive force (LCF) AlNiCo PM that can be magnetised to maintain an actuation force [11]. In the context of high-precision linear actuators, the control of remnant states governed by the hysteresis in the system strides against conventional control theory, in which the aim is generally to cancel out such non-linear behaviour. Nonetheless, this unconventional method of control has also gained traction through the development of piezoelectric transducers, such as the PIRest actuator, in which a voltage pulse is applied to a PZT ceramic in order to change its remnant mechanical strain and thereby the position offset provided by the actuator [12].

In electromagnetic position actuators, remnant state control has been furthermore investigated through the development of the Tunable Magnet Actuator (TMA). Originally proposed in [13], the TMA was designed with a similar topology as that of a C-shaped RA but replaces the mid-section of the C-core with an AlNiCo 5 Tunable Magnet (TM) within a 650-turn coil. A remnant state control algorithm based on [11] is used to change the remnant flux of the AlNiCo magnet in set intervals by intermittently inducing a saturating field to effectively remove the dependence of each proceeding magnetic state on the history of all previous states. Noting the inherent inefficiency and overshoot resulting from the saturation pulse, a control algorithm was proposed in [14] and developed in [15] called the minor-loop magnetisation state tuning (MMST) method, ensuring the smallest possible change in the required external field to reach a given state. This method has been demonstrated to have high accuracy, with a root-mean-square error (RMSE) of 9.5 mT within the tuning range of ± 1 T, although it has proven inefficient due to its slow magnetisation rate [15]. Although higher tuning rates may be achieved through the use of new control hardware and by reducing the computational complexity, faster changes in magnetisation also accentuate transient non-linearities, which are addressed in this paper to reduce thermal losses.

A further problem of the TMA is that, just as with a C-shaped RA, the actuation force is quadratically dependent on magnetic flux, making it unsuitable for accurate position control. Consequently, an alternative design based on the HRA topology, called the hybrid tunable magnet actuator, integrates HCF-PMs to produce a bi-directional and roughly linearised actuation force with respect to the TM flux (Figure 1a) [16]. However, the challenge of utilising the principle of remnant magnetic state control for position control introduces the further challenge of estimating the magnetic flux within the magnet from the measured magnetic flux in the variable air-gaps while the mover is displaced from the central position. This problem, alongside the challenge of designing a position controller, therefore, remains to be solved.

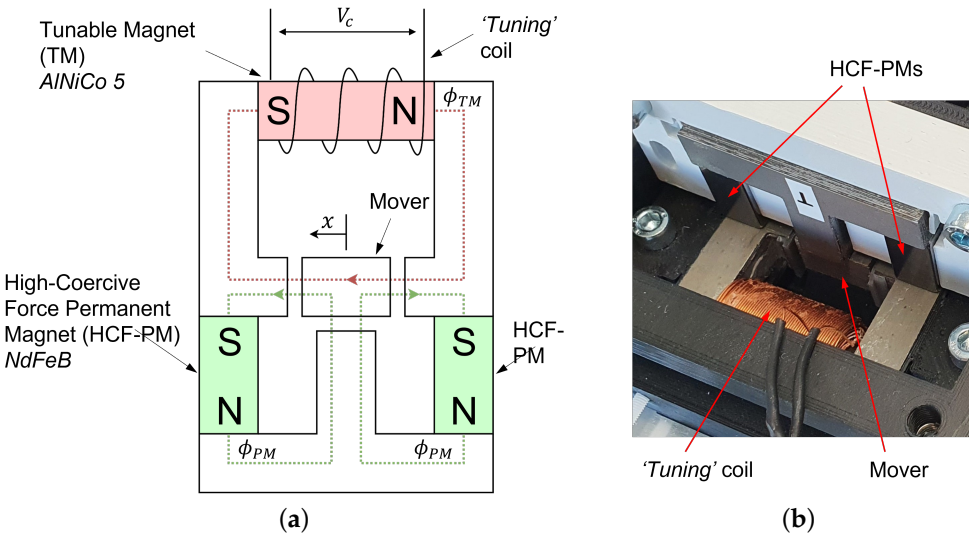

Figure 1. (**a**) Schematic of the HTMA. The HTMA includes bias flux paths (denoted by ϕ_{PM}) produced by HCF-PMs (green), which contribute to linearising the relationship between magnetic flux in TM, ϕ_{TM} (red), and the force on the mover in the x-direction, $F_{x,a}$. (**b**) Picture of the lab setup. The design in (**a**) is flipped upside-down and incorporates a 90° fold between the lower and upper halves.

This paper addresses the challenge of improving the slow tuning rate and accurately estimating the magnetic state of a TM. By combining its contributions, we demonstrate a proof-of-principle for controlling the remnant magnetisation state to enable efficient and precise quasi-static positioning. The first contribution involves the design and validation of a novel algorithm for remnant magnetic state control. This algorithm is implemented on a field programmable gate array (FPGA) and enables the TM to be tuned in the shortest possible time using the available power electronics. The second contribution outlines and validates a method for determining the magnetic flux and field within the magnet based on the mover's position and air-gap flux measurement. A lumped parameter model is also designed and used to guide this method. Lastly, the mechanical stiffness of the mover is determined, and the mover's position is experimentally characterised with respect to the remnant MS of the TM, enabling the construction of a position controller.

The organization of this article is as follows: Section 2 provides a detailed explanation of the MMST method's working principles and introduces the newly developed remnant state control algorithm. Section 3 presents an analytical model of the position actuator and is further divided into two subsections, the first of which, (Section 3.1) describes a method for estimating the magnetic state of the TM, while Section 3.2 details the characterisation of the static position of the mover at different remnant states of the TM. Moving on to Section 4, we discuss the results obtained from using the characterised behaviour to design a position control algorithm based on the MMST method. Finally, Section 5 concludes the article.

2. Improving Minor Loop Magnetisation State Tuning

The magnetic flux density of a tunable magnet, B_{TM}, is dependent on both the external field intensity, H_{TM}, and the magnetisation resulting from the alignment of magnetic moments in the material [17]. As a result, the functional dependence of B_{TM} and the magnetisation on the field input H_{TM} is governed by hysteresis, which causes the value of B_{TM} to be dependent on both the instantaneous value of H_{TM} in addition to its history of previous values. As a result, the change in B_{TM} following a series of directional changes of the field describes a series of nonoverlapping reversal curves in the B–H plane, as described in Figure 2 [18].

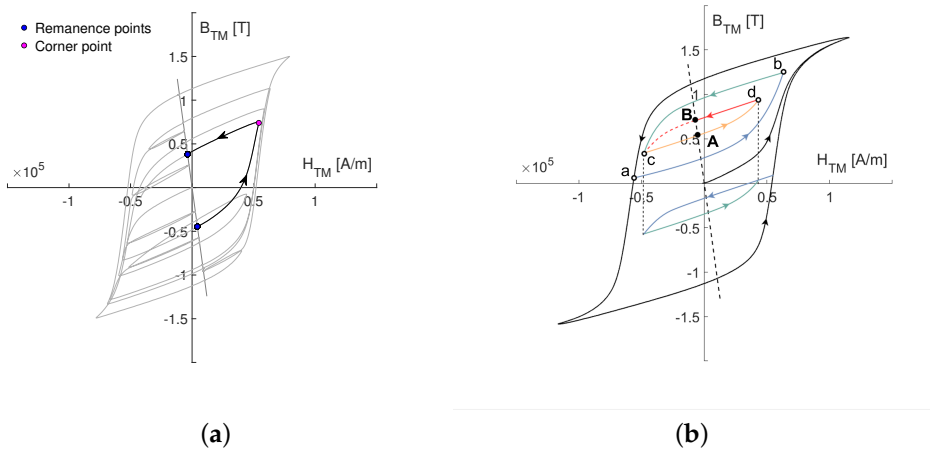

(**a**) (**b**)

Figure 2. (**a**) MMST principle of linking concurrent remnant points with a single CP. (**b**) Illustration of minor hysteresis loops, with CPs a, b, c and d linking a series of reversal curves of increasing order, ultimately crossing RPs A and B at the intersection with the load line (black dashed-line). A first-order reversal curve is generated following the field reversal at the major loop at CP a (blue line). The following green, orange, and red curves are second-, third-, and fourth-order reversal curves, respectively.

The classification of the TM as an LCF-PM means that it has a relatively low coercivity of around 50 kA m^{-1}, whereas an HCF magnet may have a coercivity on the order of 1000 kA m^{-1} [17]. For the purpose of the system considered in this paper, this allows the TM, which is consistently a 30 mm long AlNiCo 5 magnet, to be fully saturated (through the alignment of all magnetic moments) by inducing a relatively low electrical current of roughly 7 A in a 655 turn coil spanning the full length of the magnet. By varying the current whilst the magnet is between the positively and negatively saturated magnetisation states, we can change the remnant level of magnetisation and, therefore, the magnitude of B_{TM} that remains after the current is removed.

Remnant magnetisation state control is most efficiently achieved by applying a monotonic change in a magnetic field until the magnetic (H, B) state reaches the corner point (CP) to a reversal curve that intersects the proceeding remnant state, as shown in Figure 2a. As a result, that CP, together with the previous CP (just as in points c and d in Figure 2b), describe the bounds of a minor loop composed of two reversal curves that traverse the previous and the new remnant state points (RP) (points A and B), respectively. This is the formative idea of the minor-loop magnetisation state tuning method (MMST) proposed for TMAs in [14].

To prevent the estimation of CPs corresponding to remnant states along higher-order reversal curves from becoming an insurmountably complex task, J. Wiersema [15] extended the congruency-based estimation method in [19] to predict the CPs of higher-order reversal curves from first- and second-order curves. The congruency-based regularity of hysteresis describes all minor loops bounded by the same input limits as having the same shape (as illustrated by the two minor loops in Figure 2b) [18]. Although this feature is not fully preserved in magnetic materials [17], it is generally accurate to assume that curves stemming from the same reversal points are congruent [19]. Therefore, by transplanting second-order reversal curves onto higher-order curves intersecting the same RPs, a tuning method is developed that is capable of controlling the remnant magnetic flux.

The estimation method in [15] is performed offline while utilising a controller to attain a damped system response that limits the overshoot that may occur at the CPs as a result of the time delay of the controller; however, this also reduces the efficiency of the system. To improve the tuning rate and the efficiency of the system, alternative methods to reducing computational complexity should be explored, and the microcontroller must be replaced by a higher bandwidth microcontroller or an FPGA [15]. However, increasing the tuning

rate also causes eddy currents to have a greater effect on the geometry of reversal curves and, therefore, the accuracy of a congruency-based estimation as well.

The magnitude of the eddy current field $\mathbf{H_{eddy}}$ is proportional to the rate of change in magnetic flux density $\mathbf{B}$ and the conductivity of the material σ (1). An increase in the rate of magnetisation thus also increases the required magnetising field to change the flux density, causing reversal curves to expand outward along the H-axis, resulting in a so-called 'loop-widening' effect.

$$\nabla^2 \mathbf{H_{eddy}} = \sigma \frac{\partial \mathbf{B}}{\partial t}, \tag{1}$$

The rate of change in B is furthermore dependent on the current in the coil I, which depends on the inductance L. The inductance is, moreover, dependent on the reluctance of the magnetic circuit $\Re$, as seen from the derivation of the voltage (neglecting resistance) V_ϕ in a coil with N numbers of turns (2),

$$V_\phi = N\frac{d\phi}{dt} = NA\frac{\partial B}{\partial H}\frac{dH}{dt} = \frac{N^2}{\Re}\frac{dI}{dt} = L\frac{dI}{dt}, \tag{2}$$

When considering the isolated flux path through the TM in Figure 1a (red-dotted line), the total reluctance may be approximated when the mover is in the centred position ($x = 0$) by the linear expression in (3) [16].

$$\Re \approx \frac{l_{TM}}{\mu_r \mu_0 A_{TM}} + \frac{2l_g}{\mu_0 A_g}, \tag{3}$$

where l_{TM} and A_{TM} denote the length and cross-sectional area of the TM, l_g and A_g are the lengths and cross-sectional areas of the air-gaps on either sides of the mover, μ_0 is the magnetic permeability of a vacuum, and μ_r is the relative permeability of the TM. The *widening* effect on reversal curves therefore changes depending on variations in μ_r (in the range of 5 to 270, depending on the MS), causing the inductance and, thereby, the eddy current field H_{eddy} to change. The measured change in inductance throughout a minor loop intersecting the saturated and demagnetised states is illustrated in Figure 3. When provided the congruence principal and a constant voltage input, the shape of overlapping reversal curves of different orders will nonetheless be the same, as the variation in μ_r and thus the magnitude of H_{eddy} is the same throughout the curves. Consequently, to prevent variations in the measured geometry of congruent reversal curves, the possibility of controlling the voltage to prevent overshoot is eliminated.

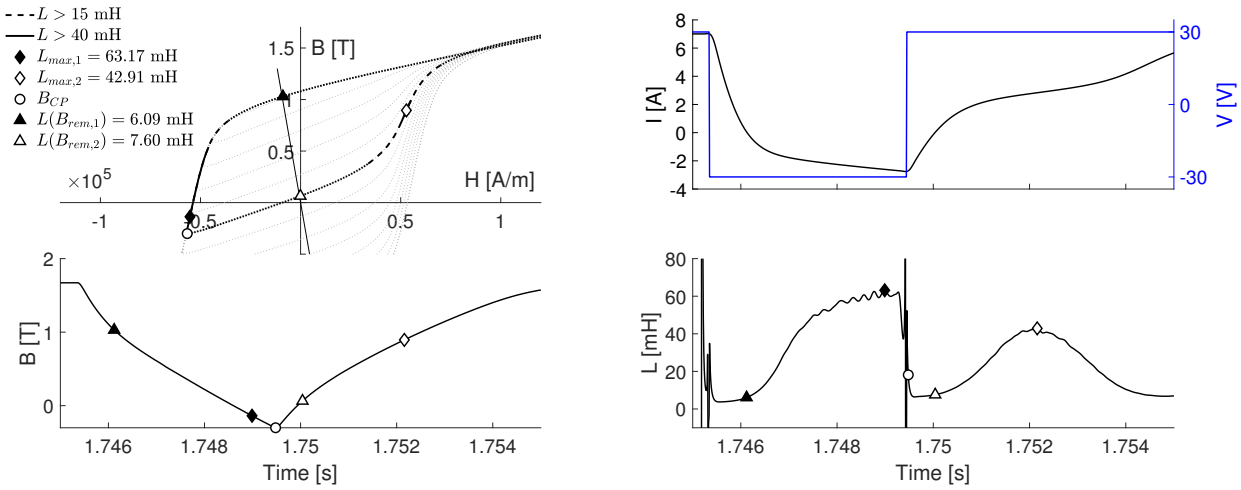

Figure 3. Measurements from tracing a hysteresis loop in the upper half of the B–H. **Top left**: B–H plane. **Bottom left**: transient change in magnetic flux density. **Top right**: change in current in and voltage across the inductor. **Bottom right**: Change in inductance throughout the traced minor loop.

In summary, without a method of accurately accounting for rate-dependent non-linearities, the problem of designing an MMST algorithm with an increased tuning rate inherently extends to the problem of mitigating the overshoot of remnant magnetisation states without the ability to modulate the voltage of the inductor. Given this extended problem definition, this article proposes an alternative method for implementing the MMST method on an FPGA in order to maximise the tuning rate and addressing the issue of overshoot.

Rather than predicting the CP corresponding to a desired remnant state, through an offline derivation of the intersection of interpolated measurements of first- and second-order curves, as in [15], this intersection can be observed in real time when the measured (H, B) state crosses a first-order reversal curve that intersects the next remnant state. This crossing point is exemplified in Figure 4. Figure 4 further illustrates that the CP can be determined at the point in time when the linearised slope of a descending first-order reversal curve (red line), α, is equal to or greater than that of the green line, β, connecting the measured (H, B)-state to the CP of that reversal curve. Hence, look-up tables were produced from the measurement data of the slope of a series of descending and ascending first-order reversal curves and (H, B) coordinates of their respective CPs along both ascending (dashed line) and descending branches of the major loop. In other words, this method of determining the CP of a given remnant state rests on the claims that (1) reversal curves are linear in the region between the previous CP and the remnant state and (2) all reversal curves intersecting the same remnant states from the same side of the B–H plane are congruent.

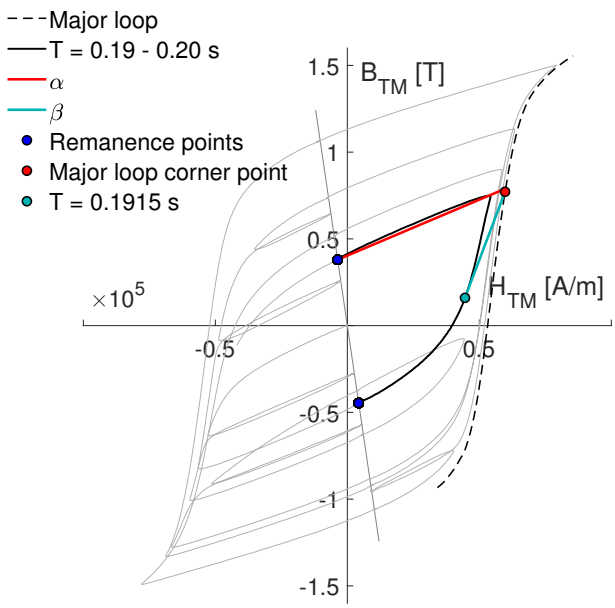

Figure 4. Method for derivation of CPs to individual remnant states. A linearised descending first-order reversal curve (red line) to the next desired remnant state (blue dot) is derived from a look-up table. The CP is determined when the slope β of the green line connecting the current (B, H) state to the CP of the linearised reversal curve (red dot) is smaller than the slope of the linearised curve α.

The control algorithm is summarised by a flow chart in Figure A1. A set of three look-up tables for the slope α and CP (H, B) coordinates are interpolated and stored in the FPGA memory from the identified ascending and descending first-order reversal curves shown in Figure A2a and Figure A2b, respectively.

Figure 5 shows the transient change in the magnetic flux density in the TM, the electric current in and voltage applied to the coil, and the resultant electrical energy of each tuning step throughout a 0.2 s run-period of the MMST algorithm. As shown, each voltage pulse

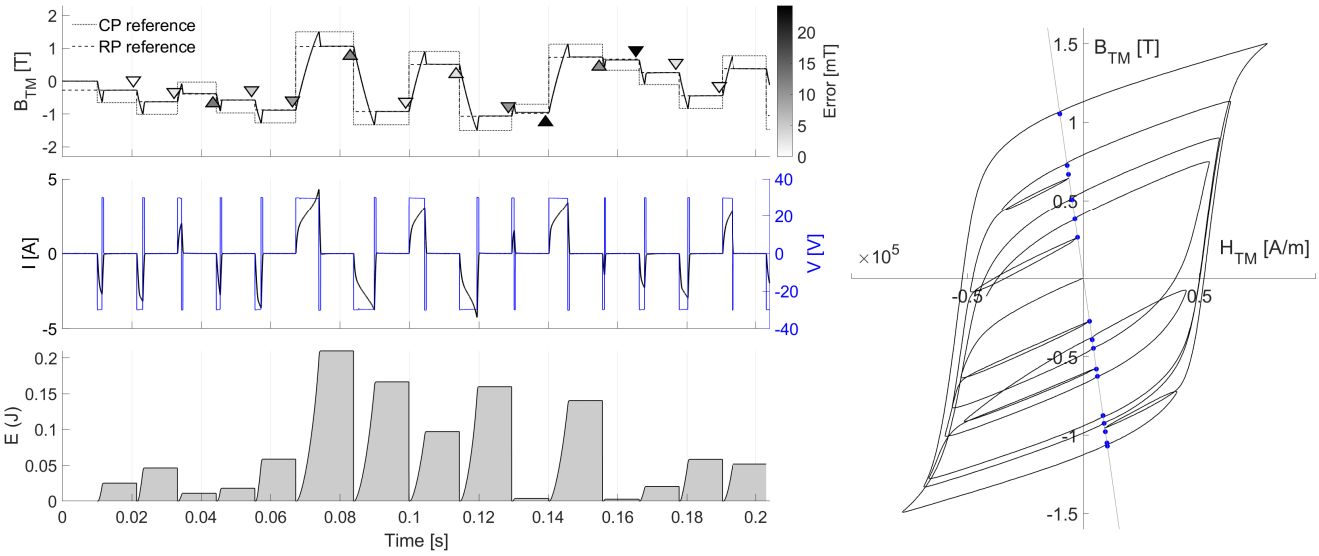

Figure 5. Minor loop magnetisation state tuning. (**Top left**): Magnetic flux density in the magnet and reference values for remnant flux and the respective CPs for each remnant state. (**Centre left**): Induced voltage and measured electric current in the inductor. (**Bottom left**): Calculated electric energy of each individual tuning step. (**Right**): B–H diagram.

is followed by a pulse of opposite amplitude to remove the current in the coil and reduce ohmic losses. Without the ability to modulate the voltage, the induced field consistently overshoots the CPs by a varying extent, depending on the rate of magnetisation, as can be seen from errors between the reference and measured magnetic flux in the top-left plot of Figure 5.

These errors are compared for a larger dataset of 2000 remnant states against the electric current in the coil at the CPs and the difference in magnetic flux density between the current and preceding RP, ΔB_{rem}, in Figure 6. The error is linearised with respect to the electric current and ΔB_{rem}, forming separate functions for the predicted error corresponding CPs in the left- and right-hand B–H plane, respectively. (These functions are captured by the row vectors $\mathbf{C}_{M^-}$ and $\mathbf{C}_{M^+}$ in the summary of the control algorithm in Figure A1), which is hence subtracted from the magnetic flux in the CP approximation in the MMST algorithm. After calibration, the mean average error is hence reduced to 0.45 mT, although the standard deviation remains roughly the same (7.19 mT). The deviation is particularly high when RPs are close together and the conjoining CPs are thus further away from the major loop, making the approximation less accurate. Consequently, the RMSE is 4.80 mT for RPs that are separated by more than 1 T and 8.05 mT for RPs that are separated by less than 1 T.

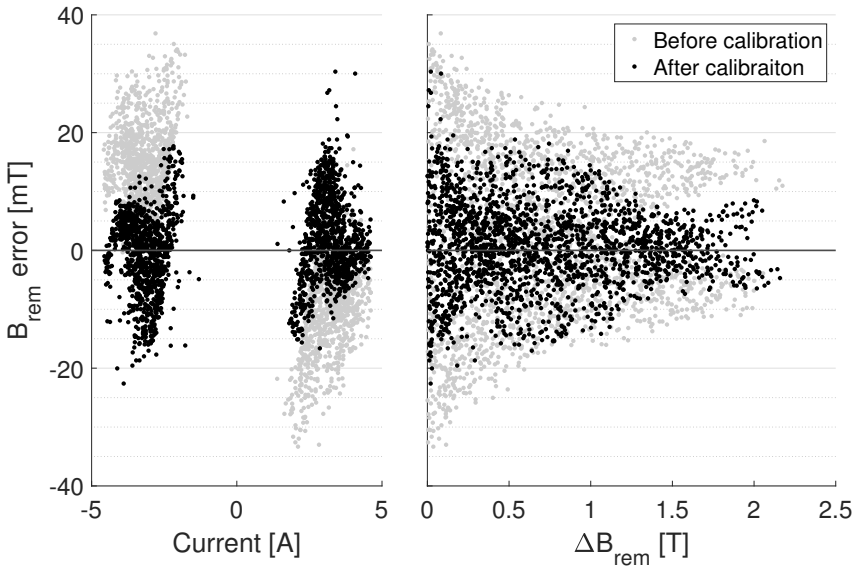

Figure 6. Steady-state error of the magnetic flux in the TM for 2000 different reference values of remnant flux when running the MMST algorithm before (grey markers) and after (black markers) overshoot compensation. After calibration, the MAE is reduced to 0.74 mT, with a standard deviation of 7.19 mT.

3. Circuit Analysis and Position Control

This section addresses the challenges regarding the realisation of a short-stroke position stage working on the principle of remnant magnetisation state control and proposes a method for determining the required and current magnetisation state of the TM. The challenges involved in achieving position control are primarily two-fold and are therefore presented in this order: (1) estimating the magnetic state within the TM from the measured magnetic flux, and (2) designing and characterising the equilibrium positions of a mechanically supported mover.

3.1. Estimation of Magnetisation State

The magnetic flux density in the TM B_{TM} is inferred from the measurement of magnetic flux density in the rightward variable air gap, B_{gr} (Figure 1a). When the mover is centrally located, and the reluctances of the opposing air-gaps are equal, this approximation can be achieved by scaling and offsetting the measurements to match the theoretical major hysteresis loop of the TM [16]. However, when the mover is displaced, resulting in a change in the air gaps' reluctances, the influence of the position on the magnetic flux in the air gap requires the approximation of the magnetic flux in the magnet to be changed (the presumption of the individually isolated flux paths in Figure 1a thus becomes inadequate). Therefore, the position sensitivity of the measurement must be isolated before the magnetisation state (H_{TM}, B_{TM}) can be determined. For this purpose, the functional dependence of B_{gr} on the mover position x is first determined from a linear lumped model of the actuator.

When considering the elements of the circuit (Figure 7a), which consist of laminated silicon steel and air gaps, it is acceptable to assume that MMF Ψ is directly coupled to magnetic flux density ϕ through reluctance $\Re$ following Hopkinson's law [1],

$$\Psi = \Re\phi, \tag{4}$$

where, assuming the magnetic properties of a given element is uniform over an area A and length l, the magnetic flux and MMF may be simplified from Ampere's current law and Gauss' law, respectively [1],

$$\Psi = Hl = NI, \qquad \phi = BA, \tag{5}$$

and the reluctance is defined as

$$\Re = \frac{l}{\mu_0 \mu_r A} \tag{6}$$

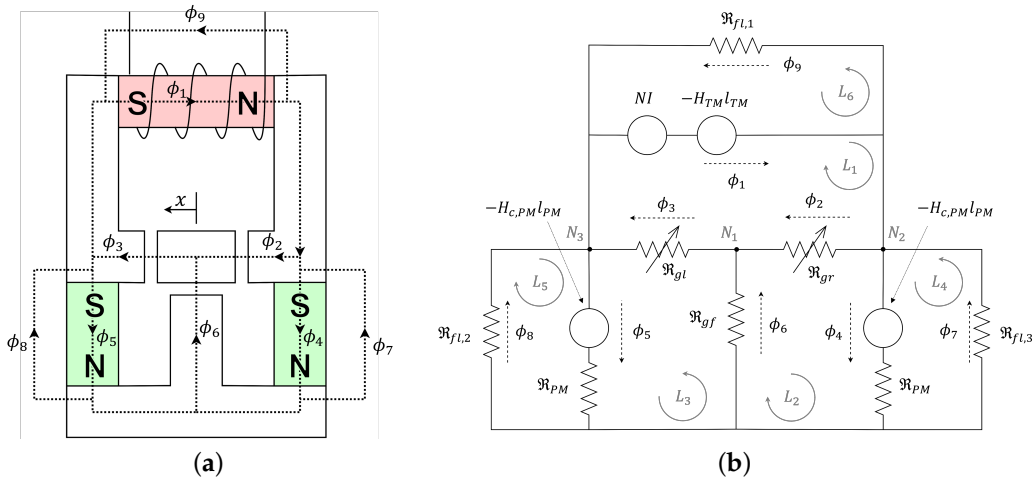

Figure 7. Lumped parameter model of the HTMA. (**a**) Illustration of the magnetic flux paths in the actuator. (**b**) Electric circuit equivalent of the magnetic circuit.

The magnetic flux through a circuit composed of several such lumped elements may be determined in analogous terms to how current in an electrical circuit is derived from Kirchoff's voltage and current laws. The MMF of m discrete sources and p inductors are summed together in closed loops, and the magnetic flux in n discrete magnetic conductors are added together at the nodes of inter-joining loops (7) [5].

$$\sum_{h=1}^{m} \Psi_h = \sum_{h=1}^{m} H_h l_h = \sum_{j=1}^{p} N_j I_j, \qquad \sum_{k=1}^{n} \phi_k = 0, \tag{7}$$

While the TM is magnetised across a range of reversal curves, the applied field is insufficient to magnetise the HCF-PMs beyond the linear region of the reversal curve at its initial remnant state. The magnetic field H_{PM} and flux density B_{PM} can thus be described by a linearisation of this curve, as defined by its relative permeability μ_r and coercive field strength $H_{c,PM}$ [3].

$$H_{PM} = \frac{B_{PM}}{\mu_0 \mu_r} + H_{c,PM} = \frac{\phi_{PM}}{\mu_0 \mu_r A_{PM}} + H_{c,PM}, \tag{8}$$

A further simplification can be made through substitution of the $\Re$ property in (6),

$$\Psi_{PM} = H_{PM} l_{PM} = \Re_{PM} \phi_{PM} + H_{c,PM} l_{PM} \tag{9}$$

thus allowing the HCF-PM to be expressed as a Theuvenin's equivalent of a series combination of a reluctance and an MMF source [9], as shown in the derivation of the electric circuit equivalent in Figure 7.

The impossibility of creating magnetic insulation results in flux leakage throughout the circuit [1]. The proportion of the magnetic flux short-circuits the magnets, and the coil is captured through the parallel circuits of reluctances $\Re_{fl,1}$, $\Re_{fl,2}$, and $\Re_{fl,3}$ (it is assumed that $\Re_{fl,2} = \Re_{fl,3}$).

Although the TM cannot be linearised, the intention is not to calculate the change in flux across a reversal curve but rather across all remnant states when no external field is applied ($I = 0$). Thereby, its reluctance can be ignored, and the solution to the variation of the field parameter H_{TM} is the magnetic flux in the circuit while the magnet is at a remnant state. The relationship between H_{TM} and B_{TM} forms a *loadline* in the B–H plane that is illustrated by the dashed line in Figures 2–5, which may be simplified by the expression in (10). The loadline is shifted along the H_{TM} axis by the field produced by the inductor ($H_{coil} = NI/l_{TM}$). The slope of the loadline c_1 is identified first experimentally such that the major loop matches the theoretical hysteresis loop of the AlNiCo magnet and can hence be used as a tuning parameter for $\Re_{fl,1}$, $\Re_{fl,2}$, and $\Re_{fl,3}$ in the analytical model.

$$B_{TM} = -c_1 \left(H_{TM} - \frac{NI}{l_{TM}} \right) \tag{10}$$

Following the rules of superposition, the lumped model of the actuator in Figure 7b is decomposed into two linear circuits, whereby one circuit considers only the MMF source of the TM, and the other considers only the two remaining MMF sources of the HCF-PMs. It thus follows that the total flux in each of the air gaps can be calculated through the summation of the fluxes from both circuits (Figure 8a). It should be noted that in the circuit of the HCF-PMs, the reluctance of the TM is approximated based on its average magnetic permeability of $\mu_r \approx 5$ at remnant states (see: Appendix A). All in all, the two lumped models are fully defined by the equations in Table A1. The magnetic fluxes $[\phi_1, \phi_2, \ldots, \phi_9]$ in Figure 7 are solved from the sets of equations pertaining to each superimposed circuit and summed together.

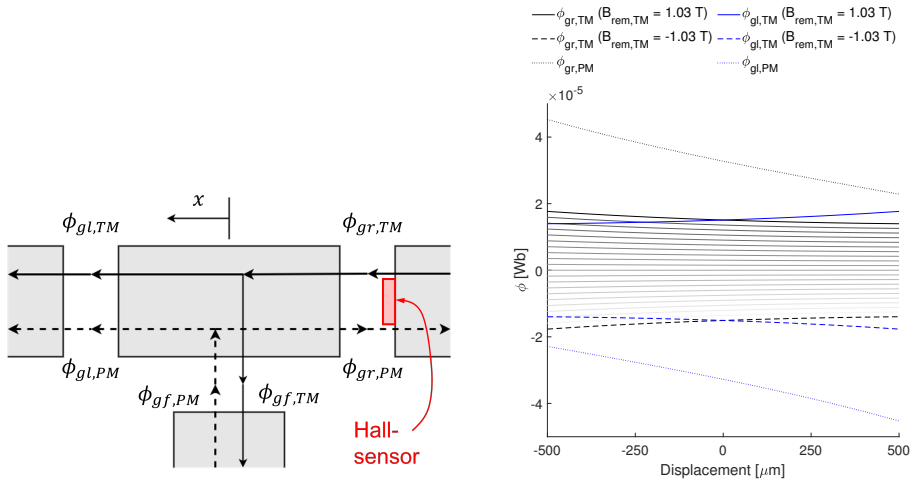

(**a**) (**b**)

Figure 8. Magnetic flux in the left and right air gaps derived in the superimposed circuits of the HCF-PMs and TM individually. (**a**) Schematic of the TM circuit (solid line) and the HCF-PM circuit (dashed line) in the air gaps. (**b**) Derived magnetic flux in the left and right air gaps (denoted by subscripts gl and gr, respectively) in the TM and HCF-PM circuits (denoted by the respective subscripts TM and PM) when the mover is displaced in the x direction and at different remnant states of the TM.

A leftward shift of the mover in the positive x direction causes the reluctance of the right air gap to increase and that of the left air gap to decrease. Logically, this causes the measurable magnetic flux in the right air gap ϕ_{gr} to decrease, as is shown to be the case for both the magnetic flux in the TM circuit $\phi_{gr,TM}$ and in the HCF-PM circuit $\phi_{gr,PM}$ in Figure 8b. The total reduction in flux ϕ_{gr} is, therefore, higher when the magnetic flux in the TM is more positive, as shown in Figure 9a, causing the change in $\phi_{gr,TM}$ with displacement to be larger. When the TM is negatively magnetised, and the direction of $\phi_{gr,TM}$ thus opposes $\phi_{gr,PM}$, the position sensitivity of $\phi_g r$ decreases.

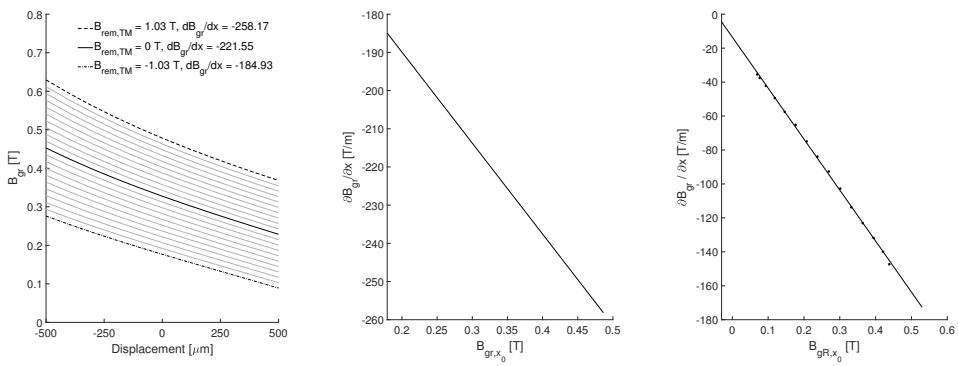

(**a**) (**b**) (**c**)

Figure 9. Position sensitivity of the measured magnetic flux ϕ_{gr}. (**a**) Summation of the magnetic flux in the right air gap of the two superimposed circuits (in Figure 8b). (**b**) Change in the displacement sensitivity of the magnetic flux density $\partial B_{gr}/\partial x$ at different remnant levels of magnetisation providing a variation of the magnetic flux density in the rightward variable gap when the mover at the origin $B_{gr,x_0} \in [0.18, 0.49]$ T. (**c**) Linear correlation of the change in $\partial B_{gr}/\partial x$ with B_{gr,x_0} from measurements.

The increasing position sensitivity of the gap flux $\partial B_{gr}/\partial x$ when the TM is positively magnetised describes a linear function. This linearity is indicated in Figure 9b, where B_{gr,x_0}

is the magnetic flux density measured when the mover is at the origin and may therefore be directly related to B_{TM} through (11), as follows:

$$B_{TM} = c_2\left(B_{gr,x_0} - B_{gr,PM,x_0}\right), \tag{11}$$

where the scale factor c_2, which, together with c_1, is defined such that the state (H_{TM}, B_{TM}) traces the major hysteresis loop of the magnet when applying a cyclic saturating field.

The linear relationship between $\partial B_{gr}/\partial x$ and B_{gr,x_0} was validated by magnetising the TM to a number of different remnant states and displacing the mover in the a range of ± 200 µm. Figure 9c shows the strong linear correlation of the experimentally obtained data, allowing $\partial B_{gr}/\partial x$ to be estimated from the position x through the equations below:

$$\frac{\partial B_{gr}}{\partial x} = -300.4x - 13.5, \tag{12}$$

Given that B_{gr} can be accurately described with respect to B_{gr,x_0} and x from

$$B_{gr} = \frac{\partial B_{gr}}{\partial x}x + B_{gr,x_0}, \tag{13}$$

we may rearrange (13) and insert the estimation of $\partial B_{gr}/\partial x$ in (12) to approximate B_{gr,x_0},

$$B_{gr,x_0} = \frac{B_{gr} + 13.5x}{-300.4x + 1} \tag{14}$$

Thus, we remove the displacement sensitivity of the measured flux density. B_{TM} can hence be derived from (11) and H_{TM} by rearranging the loadline Equation (10).

For verification, the major hysteresis loop of the TM was swept at different positions (Figure 10a), and the approximation of B_{TM} from B_{gr} and x was implemented to check the agreement of the loops. Figure 10b shows the approximation of B_{TM}. The intersection of the major loop with the B_{TM} axis at $H_{TM} = 0$ is used to evaluate the agreement of the loops. As shown in the right-hand plot in Figure 10b, the deviation of these intersections increases from the baseline when the mover is further away from the centre. Nonetheless, the error remains within 15 mT over the investigated movement range. The position sensitivity of the error appears to be higher for the intersections in the lower half of the B–H plane.

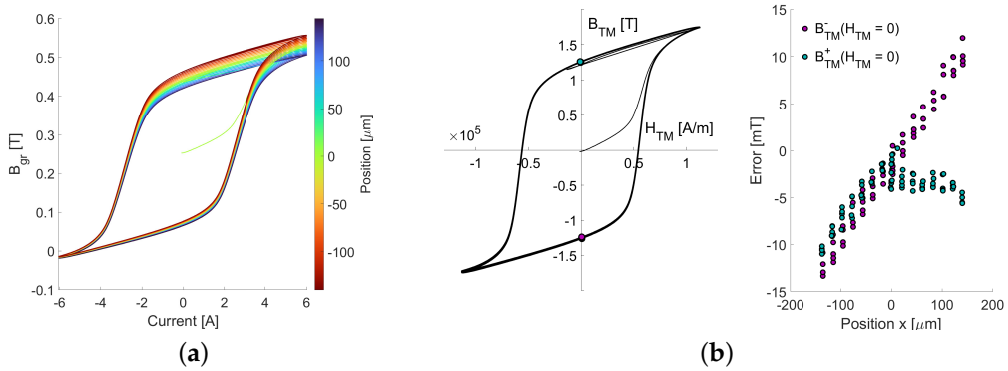

(**a**) (**b**)

Figure 10. Estimation of B_{TM} and H_{TM}. (**a**) Magnetic flux density measured in the right gap B_{gr} while the mover is displaced in the range of ± 150 µm. (**b**-left) Estimation of the magnetic flux B_{TM} and field H_{TM} in the TM from measurements in (**a**) of B_{gr} and the mover position x. (**b**-right) Position dependence of the estimation error of the loops at the B_{TM} axis intercepts with respect to the major loop measured when $x = 0$.

3.2. Design and Characterisation of Motion Stage

The mover was supported by two leaf-spring flexures in a parallel arrangement. The stiffness of this mechanism was designed such that the mover could be positioned to a stable equilibrium throughout the displacement range while also utilising the full range of remnant magnetisation states to minimise the positioning error. To obtain an indication

of the required stiffness, the actuation force was derived from the lumped model across the ranges of displacement and magnetisation states by integrating Maxwell's stress tensor across the air gap area A_g (15) [9],

$$F_{a,x} = \frac{(\phi_{gl,PM} + \phi_{gl,TM}) - (\phi_{gr,PM} + \phi_{gr,TM})}{\mu_0 A_g} = K_m(x)\phi_{TM} + k_a(x)x, \tag{15}$$

The actuation force $F_{a,x}$ may be decomposed into separate terms considering the effect of the mover's displacement x and the magnetic flux in the TM ϕ_{TM}. Due to the inclusion of the bias flux paths, both the motor constant K_m and the actuator stiffness k_a were roughly constant with respect to x [16]. The force–displacement relationship, derived from (15), is illustrated in Figure 11a for different values of B_{TM} in the tuning range of the magnet. An HRA was connected in parallel with the HTMA, providing an additional negative stiffness that, together with the stiffness of the flexure mechanism of 65 kN m^{-1}, resulted in the blue line. The equilibrium position was found at each magnetisation level at the point where the sum of all the forces was 0 N. As shown in Figure 11b, the relationship between B_{TM} and the equilibrium position of the mover follows the shape of a third-order polynomial function. Figure 11c shows the actual measured position of the mover after magnetising the TM to 161 different remnant states. The measurements were interpolated by a similar third-order polynomial, although with a shorter range than initially determined due to practical limitations.

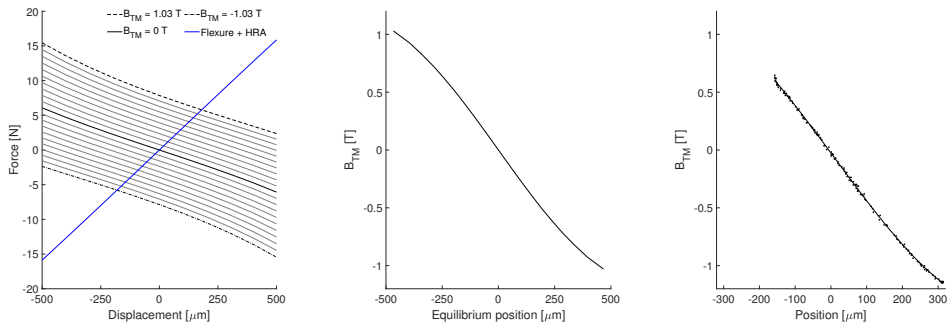

(**a**) (**b**) (**c**)

Figure 11. Equilibrium position of the actuator mover at different levels of magnetisation. (**a**) Force–displacement relationship from linear model with the TM at different remnant states. (**b**) Analytical derivation from electrical circuit equivalent. (**c**) Interpolation of the position measurements.

4. Results and Discussion

A feedforward position controller was effectively produced from the third-order polynomial function that was interpolated from the measurements (Figure 11c). By inverting the function, the required remnant flux density B_{TM} was determined for any given position x. Table 1 shows a summary of inputs, measurements, and estimations of B_{TM} while running the MMST control strategy on an FPGA to track a position reference of a random series of 150 statically held set points over a 1 s duration. The error between the reference and measured position at the end of the 1 s settling time is shown in the bottom row. The resulting RMSE is 3.98 µm over the full run. The results, thereby, successfully validate the use of in situ magnetisation for quasi-static position offsets in a short-stroke electromagnetic actuator.

Table 1. Summary of inputs and measurements during position control of the hybrid tunable magnet actuator through the minor-loop magnetisation state tuning strategy.

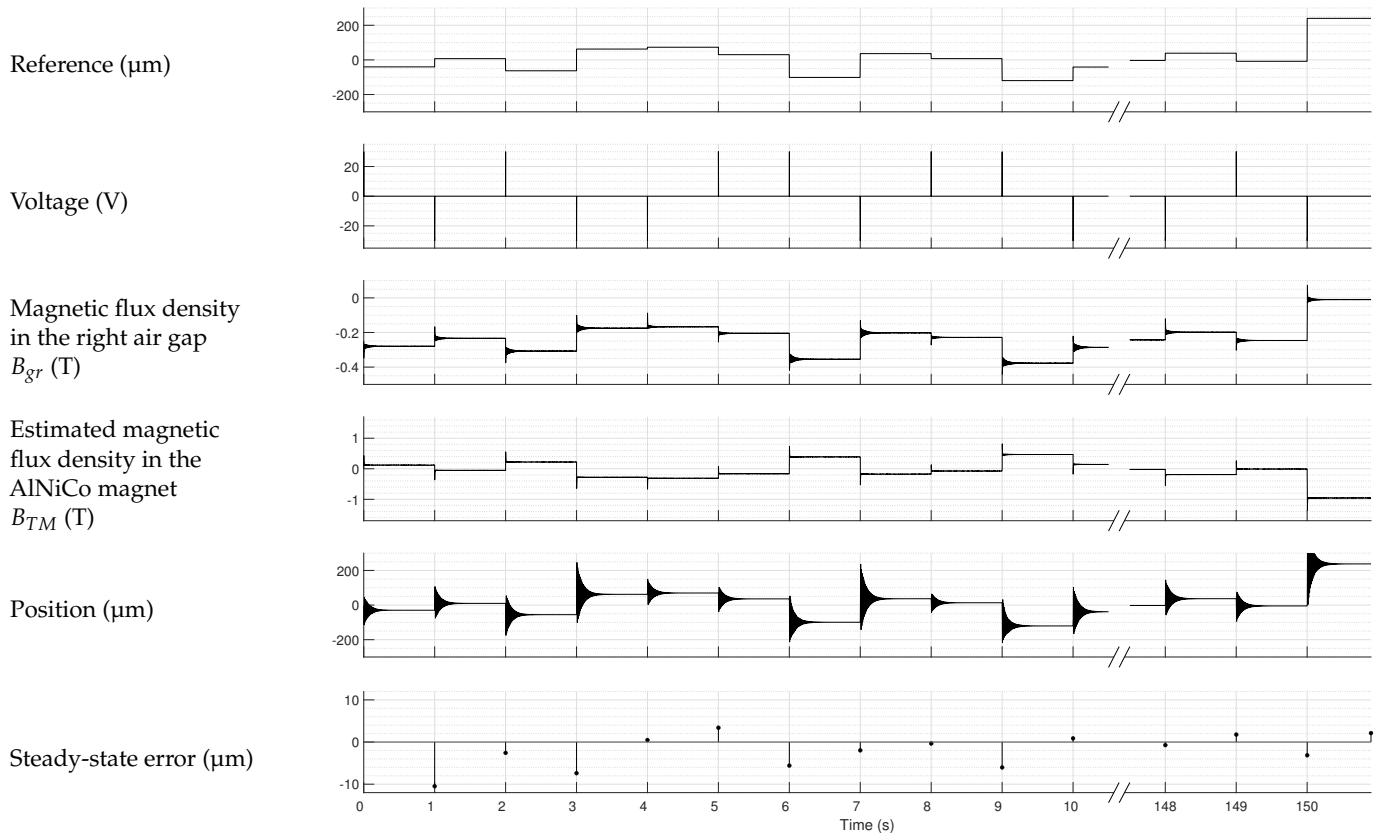

Due to inaccurate placement of the hall sensor casings, the mover was restricted from being displaced beyond −157 µm (Figure 11c). The position–displacement relationship of the HTMA follows a similar third-order polynomial function as determined analytically (Figure 11b), although the positive displacement at the lowest accessible remnant magnetisation state is 180 µm less than expected. This is presumably due to the magnetic losses being higher than anticipated or a higher mechanical stiffness than intended. Beyond more precise manufacturing techniques, the location of the hall sensor may be changed, or additional sensors may be added to improve the accuracy of the estimation of B_{TM}. The location of the hall sensor in the air gap was chosen to obtain an accurate representation of the actuation force, but this led to the measurements having a high position dependence and obstructed the mover from reaching its full positioning range.

Remnant magnetisation state control was achieved through a congruence-based MMST method, with a tuning rate that was solely limited by the maximum voltage output of the amplifier. Prediction of the overshoot of remnant magnetisation states reduced the RMSE of the remnant magnetic flux density in the tuning range of ±1.2 T to 7.22 mT. The resulting accuracy is comparable to that achieved in [15], where the rate of magnetisation was modulated through linear voltage control to prevent overshoot and reduce eddy currents. The accuracy of the presented MMST algorithm is higher when tuning between remnant magnetisation states that are further apart, as shown in Figure 6. When tuning between remnant states that are closer together, it might therefore be necessary to correct the steady-state error by inducing a series of additional magnetisation field pulses until the error is sufficiently reduced. This may, thus, warrant the design of a form of feedback controller depending on the accuracy required for a particular application, although this would reduce the efficiency of the system. Otherwise, it is probable that the application of remnant magnetic state tuning in high-precision positioning systems can be complemented

by the use of a conventional electromagnetic actuator for disturbance rejection, which may, therefore, also be used to efficiently compensate for smaller steady-state errors.

A system integrating, for instance, an HTMA and an HRA in a parallel configuration would broaden the applicability of the HTMA by leveraging the high acceleration provided by an HRA for tracking high-frequency references while taking advantage of the high efficiency of the HTMA in tracking low-frequency or quasi-static position offsets. Furthermore, it would enable the rejection of undesired dynamics, including the overshoot of the TM flux required to magnetise the TM to the CPs to their respective remnant states. Optimising the energy efficiency nonetheless hinges on the ability to accurately define the comparative energy advantage of the HTMA at different frequencies and amplitudes. Better modelling with finite element software would allow for a more comprehensive study of the change in temperature in the actuator. This could guide the actuator design and method of control for a particular application through future work, thus allowing for a more direct comparison of the thermal efficiency of existing systems.

Solving these problems would make the HTMA particularly well suited for compensating for quasi-static forces in a gravity compensator. Gravity compensator designs using HRAs allow for the compensation of constant forces with zero electrical current through the zero-stiffness behaviour of the HRA by varying the levitation height [20]. To prevent the need to change the levitation height, one must either actively adjust the arrangement of PMs within the design, such as in [4], or their remnant magnetisation state. In [11], the latter option was chosen, thus removing the need for moving parts, but the need for saturating the PM in between magnetisation pulses means that the actuator significantly overshoots each time the force must be changed. The strategy presented in this paper greatly reduces this overshoot, allowing it to be efficiently compensated for by a conventional HRA.

5. Conclusions

An energy-efficient strategy for tuning the remnant state of a permanent magnet in a range of ± 1.2 T has been described. The implemented control algorithm uses a series of look-up tables that are identified from measurements of first-order reversal curves. Through this method, the magnet is tuned to a remnant state with a single voltage pulse to an RMSE of 7.2 mT. A higher accuracy is attainable when tuning the magnet between remnant states that are further apart (for differences over 1 T, the RMSE is reduced to 4.8 mT).

Aided by the construction of a lumped-parameter model, the gap flux and position measurements are used to estimate the flux within the tunable magnet of a hybrid tunable magnet actuator within an error of ± 14 mT throughout the travel range. This allows the magnet to be accurately tuned when the mover is at any position in the travel range of -157 to 320 µm. The HTMA is controlled with a feedforward method to a series of random setpoints, achieving an RMSE of 3.98 µm.

Author Contributions: Conceptualization, E.R.; methodology, E.R.; validation E.R.; formal analysis E.R.; writing—original draft preparation, E.R.; visualization, E.R.; supervision, H.H.; writing—review and editing, A.H. and H.H. All authors have read and agreed to the published version of the manuscript.

Funding: This research received no external funding.

Data Availability Statement: The data presented in this study are available on request from the corresponding author.

Acknowledgments: E.R. would like to thank Bradley But for technical support with the lab setup.

Conflicts of Interest: The authors declare no conflict of interest.

Abbreviations

The following abbreviations are used in this manuscript:

TM	Tunable magnet
PM	Permanent magnet
HCF	High coercive force
LCF	Low coercive force
HRA	Hybrid reluctance actuator
HTMA	Hybrid tunable magnet actuator
MMST	Minor-loop magnetisation state tuning
CP	Corner point (or reversal point)
RP	Remnant state point
RMSE	Root-mean-square error

Appendix A. Lumped Parameter Model

Table A1. Superposition of linear and non-linear MMF-sources of the AlNiCo and NdFeB magnets, respectively, in Figure 7b.

TM	$L_{1,TM}:$	$\Re_{gr}\phi_2 + \Re_{gl}\phi_3 = NI - H_{TM}l_{TM}$
	$L_{2,TM}:$	$-\Re_{gr}\phi_2 + \Re_{PM}\phi_4 + \Re_{gf}\phi_6 = 0$
	$L_{3,TM}:$	$\Re_{gl}\phi_3 + \Re_{PM}\phi_5 + \Re_{gf}\phi_6 = 0$
	$L_{4,TM}:$	$\Re_{PM}\phi_4 + \Re_{fl,3}\phi_7 = 0$
	$L_{5,TM}:$	$\Re_{PM}\phi_5 + \Re_{fl,2}\phi_8 = 0$
	$L_{6,TM}:$	$\Re_{fl,1}\phi_9 = NI - H_{TM}l_{TM}$
HCF-PM	$L_{1,PM}:$	$\Re_{TM,r}\phi_1 + \Re_{gr}\phi_2 + \Re_{gl}\phi_3 = 0$
	$L_{2,PM}:$	$-\Re_{gr}\phi_2 + \Re_{PM}\phi_4 + \Re_{gf}\phi_6 = -H_{PM,c}l_{PM}$
	$L_{3,PM}:$	$\Re_{gl}\phi_3 + \Re_{PM}\phi_5 + \Re_{gf}\phi_6 = -H_{PM,c}l_{PM}$
	$L_{4,PM}:$	$\Re_{PM}\phi_4 + \Re_{fl,3}\phi_7 = -H_{PM,c}l_{PM}$
	$L_{5,PM}:$	$\Re_{PM}\phi_5 + \Re_{fl,2}\phi_8 = -H_{PM,c}l_{PM}$
	$L_{6,PM}:$	$\Re_{TM,r}\phi_1 + \Re_{fl,1}\phi_9 = 0$
ϕ	$N_1:$	$\phi_2 - \phi_3 + \phi_6 = 0$
	$N_1:$	$\phi_1 - \phi_2 - \phi_4 + \phi_7 - \phi_9 = 0$
	$N_1:$	$-\phi_1 + \phi_3 - \phi_5 + \phi_8 + \phi_9 = 0$

Appendix B. MMST Algorithm

Figure A1 is a flow chart illustrating the implemented logic for the 'tuning' process from one remnant magnetisation state to another. The interpolated CP (H, B) coordinates and slope α of a series of the first order are stored on the FPGA in 2 sets of 3 look-up tables for the ascending (M^+) and descending (M^-) reversal curves, respectively.

The interpolated overshoot of remnant flux set-points, from Figure 6, is expressed as a function in terms of the electric current at the corresponding CP I and the difference in magnetic flux density between the previous and the current remnant state set point, ΔB_{set}. The predicted flux error is added to the magnetic flux density of the CP, as provided by either look-up table.

For example, for a remnant state being accessed through an ascending reversal curve in the left-hand B–H plane, the magnetic flux density at the coordinate position of the corresponding linearised first-order reversal curve is offset by the value derived from multiplying the row-vector C_{M^+} (containing the coefficients of the function for the predicted error) with the measured electric current and ΔB_{set}.

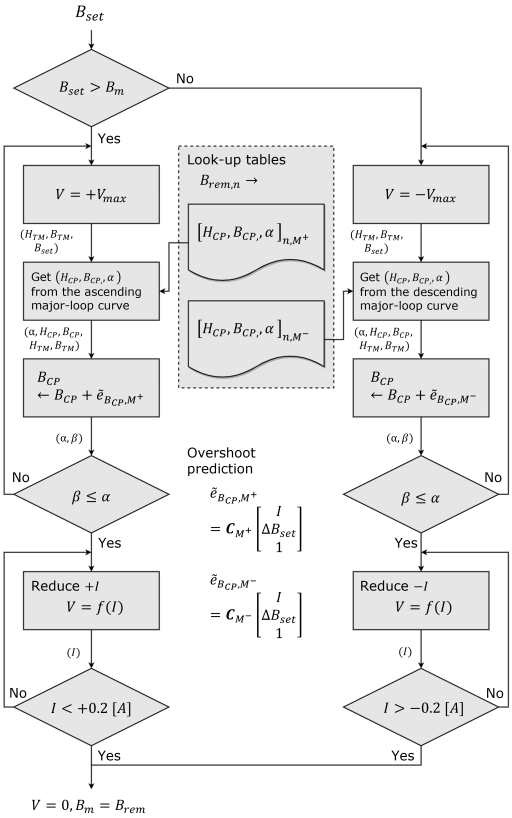

Figure A1. Flow chart of the minor-loop magnetisation state tuning algorithm.

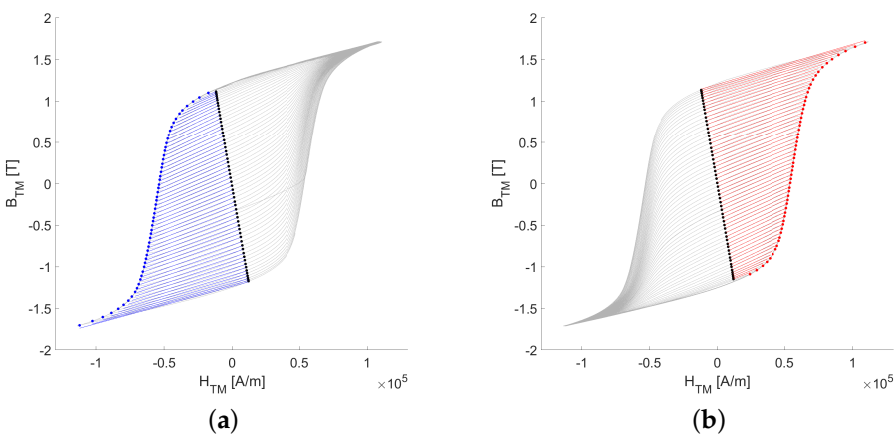

Figure A2. Look-up tables identified from measurements of reversal curves. (**a**) Ascending first-order reversal curves. (**b**) Descending first-order reversal curves.

References

1. Schmidt, R.M.; Schitter, G.; van Eijk, J. *The Design of High Performance Mechatronics*, 3rd ed.; Delft Univerity Press: Delft, The Netherlands, 2020.
2. Ito, S.; Schitter G. Comparison and Classification of High-Precision Actuators Based on Stiffness Influencing Vibration Isolation. *IEEE/ASME Trans. Mechatron.* **2016**, *21*, 1163–1178. [CrossRef]
3. Hamelinck, R.F.M.M. Adaptive Deformable Mirror: Based on Electromagnetic Actuators. Ph.D. Thesis, TU Eindhoven, Eindhoven, The Netherlands, 2010.
4. Raab, M.; Hutter, M.; Kazi, A.; Schinkoethe, W.; Gundelsweiler, B. Magnetically Levitated Linear Drive Using an Active Gravity Compensation Based on Hybrid Shape Memory Actuators. *IEEE/ASME Trans. Mechatron.* **2021**, *26*, 1380–1391. [CrossRef]
5. Vrijsen, N.H.; Jansen, J.W.; Lomonova, E.A. Comparison of linear voice coil and reluctance actuators for high-precision applications. In Proceedings of the 14th International Power Electronics and Motion Control Conference EPE-PEMC 2010, Ohrid, Republic of North Macedonia, 6–8 September 2010; pp. S3-29–S3-36. [CrossRef]

6. Ito, D.; Troppmair, S.; Lindner, B.; Cigarini, F; Schitter, G. Long-Range Fast Nanopositioner Using Nonlinearities of Hybrid Reluctance Actuator for Energy Efficiency. *IEEE Trans. Ind. Electron.* **2019**, *66*, 3051–3059. [CrossRef]
7. Ito, D.; Cigarini, F; Schitter, G. Flux-Controlled Hybrid Reluctance Actuator for High-Precision Scanning Motion. *IEEE Trans. Ind. Electron.* **2020**, *67*, 9593–9600. [CrossRef]
8. Liu, X.; Dong, J.; Du, Y.; Shi, K.; Mo, L. Design and Static Performance Analysis of a Novel Axial Hybrid Magnetic Bearing. *IEEE Trans. Magn.* **2014**, *50*, 1–4. [CrossRef]
9. Kluk, D.J. An Advanced Fast Steering Mirror for Optical Communication. Master's Thesis, Massachusetts Institute of Technology, Cambridge, MA, USA, 2007.
10. Knaian, A.N. Electropermanent Magnetic Connectors and Actuators: Devices and Their Application in Programmable Matter. Ph.D. Thesis, Massechusetts Institute of Technology, Cambridge, MA, USA, 2010.
11. Hüfner, T.; Radler, O.; Ströhla, T.; Sattel, T.; Wesselingh, J.; Vogler, A.; Eicher, D. A note on electromagnetic gravity compensation actuators based on soft electro-permanent magnets for adjustable reluctance force. In Proceedings of the 17th International Conference of the European Society for Precision Engineering and Nanotechnology, Hannover, Germany, 29 May–2 June 2017; pp. 149–150.
12. Reiser, J.; Marth, H. PIRest Technology—How to Keep the Last Position of PZT Actuators without Electrical Power. In Proceedings of the ACTUATOR 2018: 16th International Conference on New Actuators, Bremen, Germany, 25–27 June 2018; pp. 1–4.
13. Viëtor, S.G.; Spronck, J.W.; HosseinNia, S.H. Tunable Magnets: Modeling and validation for dynamic and precision applications. In Proceedings of the Conference on Precision Mechatronics, Sint Michielsgestel, The Netherlands, 4–5 September 2018.
14. Meijer, R. Tunable Magnets: Dynamic Flux-Feedback Compensation Methods for Improved Magnetization State Tuning Performance and Minor-loop Magnetization State Tuning for the Validation and Reduction of the Break-Even Tuning Interval. Master's Thesis, TU Delft, Delft, The Netherlands, 2021.
15. Wiersema, J.D. Hysteresis Modelling for Efficient and Accurate Magnetization State Tuning. Master's Thesis, TU Delft, Delft, The Netherlands, 2022.
16. Hoekwater, W. Design of a Linearized Force-Flux Tunable Magnet Actuator. Master's Thesis, TU Delft, Delft, The Netherlands, 2022.
17. Bertotti, G. *Hysteresis in Magnetism: For Physicists, Materials Scientists, and Engineers*, 1st ed.; Academic Press: Santa Clara, CA, USA, 1998.
18. Mayergoyz, I.D. *Mathematical Models of Hysteresis and Their Applications*, 2nd ed.; Academic Press: Baltimore, MD, USA, 2003.
19. Zeinali, R.; Krop, D.C.J.; Krop, E. Comparison of Preisach and Congruency-Based Static Hysteresis Models Applied to Non-Oriented Steels. *IEEE Trans. Magn.* **2020**, *56*, 1–4. [CrossRef]
20. Stadler, G.; Csencsics, E.; Ito, S.; Schitter, G. High Precision Hybrid Reluctance Actuator With Integrated Orientation Independent Zero Power Gravity Compensation. *IEEE Trans. Ind. Electron.* **2022**, *69*, 13296–13304. [CrossRef]

Disclaimer/Publisher's Note: The statements, opinions and data contained in all publications are solely those of the individual author(s) and contributor(s) and not of MDPI and/or the editor(s). MDPI and/or the editor(s) disclaim responsibility for any injury to people or property resulting from any ideas, methods, instructions or products referred to in the content.